Draft version November 16, 2025
Typeset using LaTeX default style in AASTeX631

High Precision Calibration of an Operational Amplifier based High-Input-impedance Receiver in the 21-cm Global Spectrum Experiment

Cong Zhang,[1,2] Jiaqin Xu,[1,2] Jiacong Zhu,[1,2] Kai He,[1] Shijie Sun,[1] Suonanben,[1] Shenzhe Xu,[1]
Jeffrey B. Peterson,[3] Fengquan Wu*,[1] and Xuelei Chen*[1,2]

[1]*State Key Laboratory of Radio Astronomy and Technology, National Astronomical Observatories Chinese Academy of Sciences, Beijing 100101, China*

[2]*School of Astronomy and Space Science, University of Chinese Academy of Sciences, Beijing 100049, China*

[3]*McWilliams Center for Cosmology, Carnegie Mellon University, Department of Physics, 5000 Forbes Ave, Pittsburgh, PA 15213, USA*

ABSTRACT

The 21-cm line of neutral hydrogen offers an excellent probe to the Cosmic Dawn and the Epoch of Reionization. In a 21-cm global spectrum experiment, a single wide beam antenna is used to make a high precision measurement of the all-sky averaged signal. However, the relative frequency range of such a system is often limited to one octave, as it is difficult to design an antenna with a nearly constant impedance matched to the receiver (usually 50-Ohm) over wider range. This limits its sensitivity to models where the 21cm feature is broad. In this paper, we investigate a high-impedance design, where an operational amplifier is employed as the first stage of the receiver, with impedance much higher than the antenna. Such a receiver does not rely on the impedance-matching of the antenna over wide frequency range to achieve uniform power transfer, instead it measures the voltage of the input signal, thereby circumvents the limitations imposed by impedance matching. We focus on the high-precision calibration method of this receiver design. Building on the classical signal model of the operational amplifier, we develop a model that improves accuracy by at least two orders of magnitude. Using this model, we designed a high precision calibration method with multiple resistance calibrators, and built a prototype for validation. Laboratory experiments demonstrate that after calibration, the measurement accuracy of this system reaches approximately 30 mK, sufficient for application in the 21cm global spectrum experiments.

Keywords: Neutral Hydrogen — Cosmic Dawn — Operational Amplifier

1. INTRODUCTION

The hyperfine transition of neutral hydrogen (HI) from the high-energy state to the low-energy state releases a photon with wavelength of 21-cm. Although the probability of this transversion is extremely low, a large number of diffused neutral hydrogen atoms made it possible to detect the 21-cm signal from the early universe[1; 2]. One way to detect this signal from the high redshift Universe is to employ large radio telescope arrays to detect the fluctuating signal, either by direct tomographic observation, for example by the upcoming Square Kilometer Array (SKA, [3]), or by a statistical detection in the spatial fluctuation power spectrum, for example by the the ongoing experiments such as the Hydrogen Epoch of Reionization Array (HERA, [4]), the Low-Frequency Array (LOFAR, [5]), the Murchison Widefield Array (MWA, [6]) and the Giant Metrewave Radio Telescope (GMRT, [7]), and the 21 Centimeter Array (21CMA, [8]). However, so far positive detection has not been achieved. Another approach is to detect the 21-cm global spectrum. This sky-average 21-cm spectrum exhibits the net emission or absorption features, contingent on whether the spin temperature of HI atoms exceeds or is below that of the cosmic microwave background temperature at that epoch. These spectral signatures from the primordial universe serve as a powerful tool for probing the Cosmic Dawn (CD) and the Epoch of Reionization (EoR)[9; 10; 11; 12; 13]. Compared to the telescope arrays, this approach requires only a single antenna, offering notable advantages in its simplicity. Many ground-based global spectrum experiments have been deployed currently, such as the Experiment to Detect the Global Epoch-of-Reionization Signature (EDGES,[14]), the Shaped Antenna measurement of the background RAdio Spectrum (SARAS, [15]), the Sonda Cosmológica de las Islas para la Detecciónde Hidrógeno Neutro (SCI-HI, [16]), the Probing

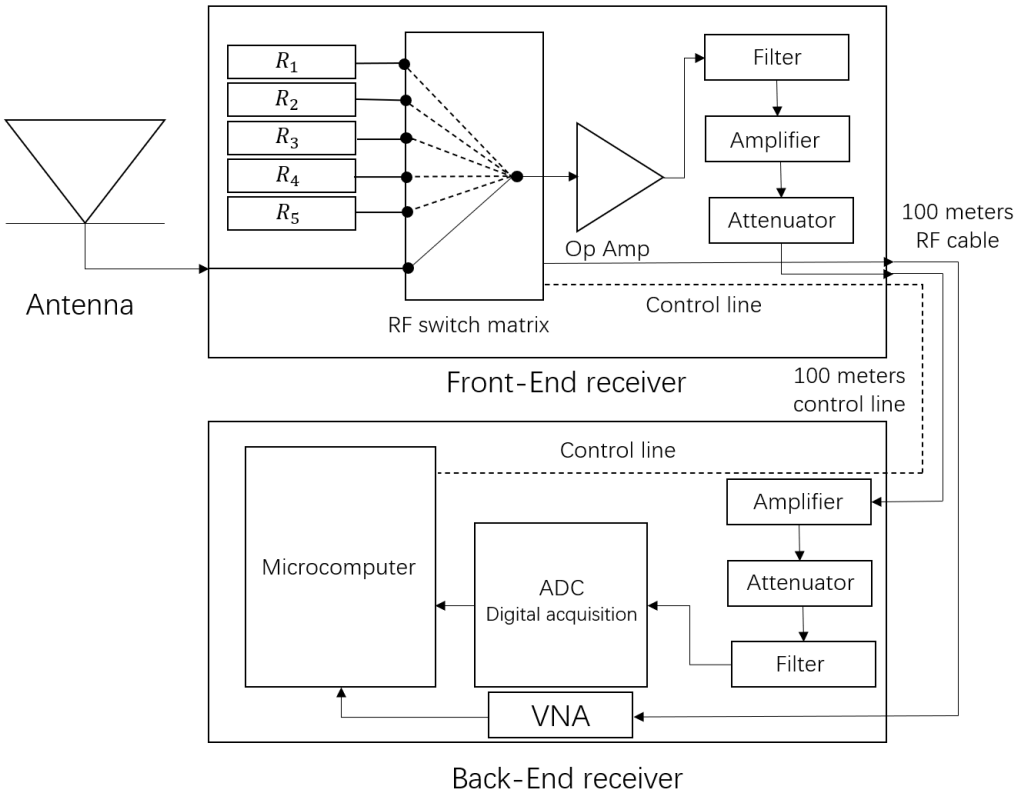

Figure 1. Block diagram of high-impedance global spectrum system.

Radio Intensity at high-z from Marion (PRIzM, [17]), the Large-Aperture Experiment to Detect the Dark Age (LEDA, [18]) and the Radio Experiment for the Analysis of Cosmic Hydrogen (REACH, [19; 20]), the Broadband Instrument for Global HydrOgen ReioNization Signal (BIGHORNS, [21]), the Large-aperture Experiment to Detect the Dark Age (LEDA, [22]), Cosmic Twilight Polarimeter (CTP, [23]), and Mapper of the IGM Spin Temperature (MIST, [24]). Besides conducting such experiments on the ground, there are a number of experiments have been proposed on the far side of the Moon, including the Discovering the Sky at the Longest wavelength (DSL, also know as "Hongmeng Project", [25; 26; 27]), the Dark Ages Radio Explorer (DARE, [28]), the Dark Ages Polarimeter PathfindER (DAPPER, [29]), the Probing ReionizATion of the Universe using Signal from Hydrogen (PRATUSH, [30]) and CosmoCube[31; 32]. These lunar-based experiments, which circumvent problems associated with ionospheric effects, can capture lower-frequency signals below 30 MHz from the cosmic dark ages. More importantly, by leveraging the Moon's shield against artificial radio frequency interference (RFI), these experiments will produce cleaner 21-cm spectra.

Most global spectrum experiments need to maintain impedance matching between the antenna and receiver to ensure maximum power transfer. However, as the frequency changes, the impedance of the antenna changes, and impedance matching in a frequency band beyond one octave is very challenging. The cosmic dawn 21-cm spectral feature in the global spectrum is typically not very narrow, in some cases the breadth of the feature may approach or even exceed one octave in frequency range, and can only be detected with systems that works on broader bandwidth [11]. One possible solution is to give up on impedance matching, instead employing a high-impedance system to achieve a smooth and nearly flat response, e.g. by using an operational amplifier as the first stage of the receiver. Over recent decades, the gain bandwidth product (GBP) of operational amplifiers have increased, extending their usable frequency range substantially. Leveraging on the extremely high input impedance of the operational amplifier, we can measure the voltage signals instead of the power signal,thus avoiding the bandwidth limitations imposed by impedance matching. Both the broader frequency range and the smooth response enable better fitting to the smooth Galactic foreground spectrum, thereby enhancing the precision of foreground subtraction.

The high-impedance global spectrum system comprises an antenna, a front-end analog receiver, and a back-end digital receiver, as illustrated schematically in Figure 1. For the antenna, we have tested several variants, for the

results presented in this work, a disc-cone design has been used. The antenna is placed on a conducting grounding plane, to simplify the radiation pattern and to mitigate the complications arising from the complicated reflections by different layers of the ground soil. To realize this conducting ground plane, radial grounding wires are laid beneath the antenna. The front-end analog receiver uses a first-stage operational amplifier, with the calibration system placed between the antenna and amplifier, which is the primary focus of this paper. The back-end digital receiver employs an analog-to-digital converter (ADC) to digitize the analog signals, which are subsequently stored in a microcomputer. For global spectrum measurements, a 100-meter radio frequency (RF) cable separates the front-end from the back-end, reducing digital interference in the received signals.

Before extracting the 21-cm signal, a global sky temperature spectrum must be obtained. To accurately recover the sky temperature, it is essential to calibrate the system during the measurement process. However, the extremely high-input-impedance of the operational amplifier renders existing power transmission signal models ineffective. For instance, the noise wave theory used in the EDGES experiment decomposes amplifier noise into forward and backward propagating power components [33; 34]. This theory fully accounts for mismatch effects in power transfer structures, providing an accurate signal model for matched or partially mismatched systems. But in our system, which is the cases of nearly complete mismatch, almost no power is delivered to the operational amplifier, the accuracy of this power transfer model is severely degraded. Instead, a voltage signal model for the operational amplifier must be used. However, the classical operational amplifier models neglect high-frequency circuit effects and are only applicable in low-frequency scenarios. Therefore, it is necessary to develop a model suitable for the frequency range of global spectrum experiments, which is the main aim of the present work.

This paper focuses on the calibration method for the high-impedance system. By analyzing signal propagation effects and operational amplifier noise in the system, a comprehensive signal model is established. Based on this model, a high precision calibration method is designed to calibrate system parameters and antenna temperatures in real time. To validate the calibration performance, we substitute the antennas with a resistor in laboratory experiment and use this method to recover the physical temperature of this resistor.

This paper is structured as follows: Section 2 analyzes operational amplifier signal model in a traditional way; Section 3 builds up our new signal model; and Section 4 presents our calibration method. Section 5 presents the results of the laboratory experiment, and the final section concludes the study.

2. CLASSICAL SIGNAL ANALYSIS OF OPERATIONAL AMPLIFIER

In global spectrum experiments, the received sky radiation consists of the foreground, dominated by the Galactic synchrotron radiation with a smooth power-law spectral shape, and the faint 21-cm signal, which is characterized by absorption or emission features. These distinct spectral features enable subtraction of the smooth foreground spectrum, allowing extraction of the 21-cm signal. However, system noise may introduce spectral structures which could interfere with the extraction of the true 21-cm signal. Therefore, precise calibration is required to eliminate the system noise. Given that the high-impedance system employs an operational amplifier as the first stage, which dominates the receiver noise, accurate modeling of the operational amplifier is essential.

The operational amplifier (op amp) is an integrated circuit incorporating multiple field-effect transistors (FETs). The non-inverting input peripheral circuit for the amplifier used in our experiment is shown in Figure 2. The op amp is powered up through port 2 (connecting to ground) and port 5 (connecting to voltage source V_s+). The RF input (antenna or calibrator source) is connected to one input terminal (port 3) of the op amp, and R_r serves as a grounding resistor for tuning the input impedance. The output terminal (port 1) is connected to the other input terminal (port 4) via a resistor R_f to form a negative feedback loop, and these are connected to the ground through a resistor R_g. The high input impedance of the op amp ensures that negligible current enters the input terminals, resulting in amplification of the voltage signal rather than power. The voltage referenced to the output is given by

$$E_{\rm out} = A_v E_{\rm in}, \qquad A_v \equiv 1 + \frac{R_f}{R_g}. \tag{1}$$

Here, A_v represents the closed-loop voltage gain of the operational amplifier, which is approximately 6.73 in our design. The output is linked to the subsequent amplification stages, which still require impedance matching to ensure efficient power transfer. Given the inherently low output impedance of the op amp, a 50Ω resistor is placed at the output of the circuit to provide impedance matching and to convert the amplified voltage signal into a power signal for the subsequent stages of the receiver.

The received powers are however related to the voltages, in the system,

$$P_{in} \propto E_{in}^2, \qquad P_{out} \equiv gP_{in} \propto gE_{in}^2,$$

where g denotes the system power gain, E_{in}^2 represents the total input voltage composed by the signal front of op amp and system noise. Since the noise from subsequent stages is not amplified by preceding stages, its contribution to the overall system noise decreases progressively along the signal chain. For example, in the prototype model we built, the second stage employs a Mini-Circuits ZKL-1R5+ amplifier, which has a typical noise figure of 3 dB. The second stage noise figure contribution referred to the input, calculated by $\frac{F_2-1}{A_v^2}$, is only approximately 0.055dB. Therefore, the first-stage op amp primarily dominates the total system noise.

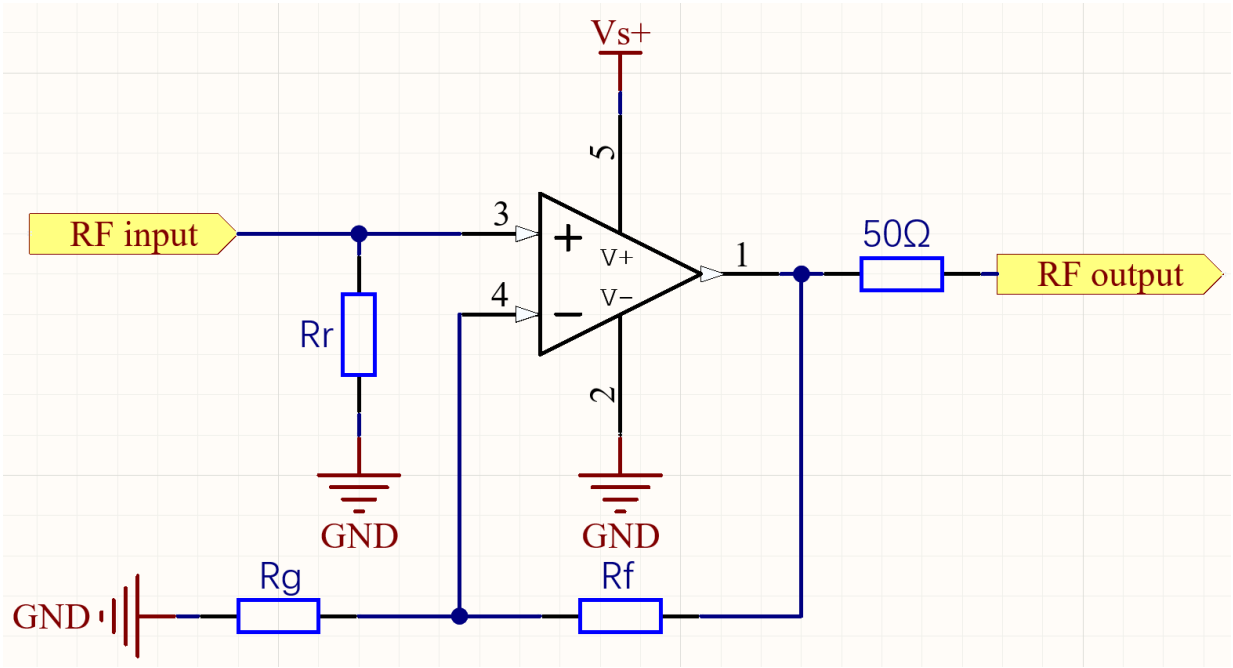

Figure 2. Diagram of a non-inverting operational amplifier circuit. The non-inverting input (port 3), inverting input (port 4), output (port 1), and power supplies (ports 2 and 5) are shown. For single-supply operation, port 2 is grounded. The feedback resistors R_g and R_f determine the closed-loop gain, while the parallel input resistor R_r adjusts the input impedance.

We now consider the noise in the op amp. Figure 3 depicts the model of the op amp circuit. In this model, the noise generated by the interior of the op amp is equivalently represented by an ideal op amp, two current sources (I_n, I_i), and one voltage source (E_n) [35; 36]. I_n denotes the non-inverting noise current source, I_i stands for the inverting noise current source, and E_n signifies the noise voltage source at the non-inverting input. Noise also arise from the peripheral circuitry of the amplifier, where E_r, E_f and E_g represents the thermal noise generated by the resistors R_r, R_f and R_g, respectively. Additionally, there is the noise of the input source, denoted by E_a. The equivalent signal model at the input terminal of the amplifier can be formulated as follows:

$$\begin{aligned}\langle E^2\rangle = \langle E_a^2\rangle \left(\frac{R_r}{R_a+R_r}\right)^2 + \left[\langle E_r^2\rangle \left(\frac{R_a}{R_a+R_r}\right)^2 + \langle I_n^2\rangle \left(\frac{R_aR_r}{R_a+R_r}\right)^2 + \langle E_n^2\rangle\right] \\ + \left[\langle E_g^2\rangle \left(\frac{R_f}{R_f+R_g}\right)^2 + \langle E_f^2\rangle \left(\frac{R_g}{R_f+R_g}\right)^2 + \langle I_i^2\rangle \left(\frac{R_fR_g}{R_f+R_g}\right)^2\right], \end{aligned} \tag{2}$$

here the angular bracket $\langle\rangle$ denotes the average. As the averaged quantities are parameters associated with the equivalent model of the op amp and can be treated as constant within a short duration, we will also use the same symbol to represent the model value, e.g. use I_n, I_i, E_n to represent $\sqrt{\langle I_n^2\rangle}$, $\sqrt{\langle I_i^2\rangle}$, and $\sqrt{\langle E_n^2\rangle}$ respectively. The thermal noise of the resistors are given by the Johnson-Nyquist relation, $\langle E^2\rangle = 4RkT$, where R is the resistance, k

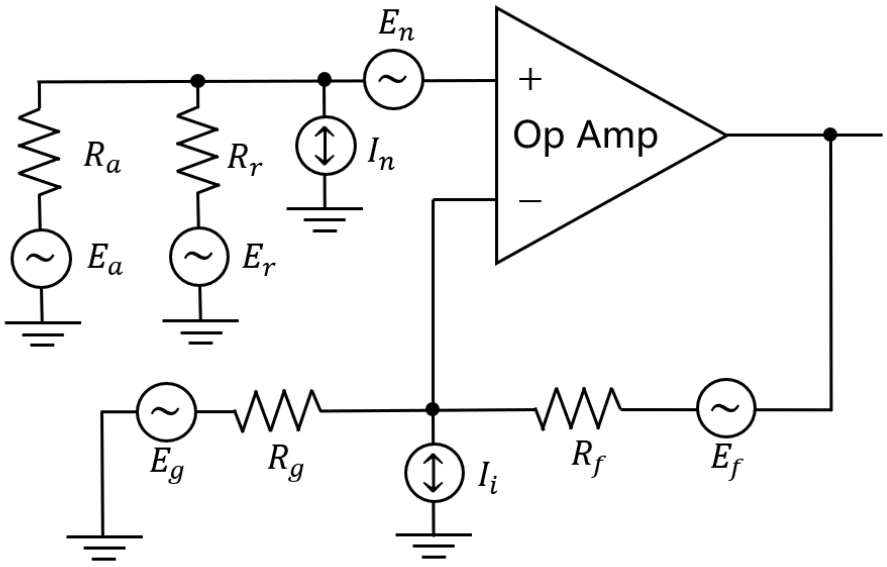

Figure 3. The classical model of high-impedance operational amplifier circuit. The internal noise of the amplifier is modeled as two current sources and a voltage source, while the resistors in the surrounding circuitry generate a thermal noise.

the Boltzmann constant, and T the ambient temperature of the resistor [37]. We then have

$$\langle E^2 \rangle = 4R_a kT \left(\frac{R_r}{R_a+R_r}\right)^2 + \left[4R_r kT \left(\frac{R_a}{R_a+R_r}\right)^2 + I_n^2 \left(\frac{R_a R_r}{R_a+R_r}\right)^2 + E_n^2\right] + \left[4R_g kT \left(\frac{R_f}{R_f+R_g}\right)^2 + 4R_f kT \left(\frac{R_g}{R_f+R_g}\right)^2 + I_i^2 \left(\frac{R_f R_g}{R_f+R_g}\right)^2\right], \tag{3}$$

where the input voltage of op amp is decomposed into three components: the first term on the right hand side (r.h.s.) represents the contribution from the input source, the second corresponds to the input noise at the non-inverting terminal of the op amp, and the third accounts for the input noise at the inverting terminal.

To simplified the signal model of amplifier, certain noise terms in the amplifier circuit can be combined to streamline the solution process. Since both the input noise at the inverting terminal of the third component and $\langle E_n^2 \rangle$ are independent of the source input, they are combined into a single total voltage noise E_{noise} for simplicity. The thermal noise of the input resistor $4R_r kT \left(\frac{R_a}{R_a+R_r}\right)^2$ can be equivalently represented as a parallel current source with magnitude $\sqrt{\frac{4kT}{R_r}}$ at the non-inverting input. The total noise current I_{noise} is then defined as the superposition of this equivalent noise current and the intrinsic noise current.

The simplified signal model of the operational amplifier is depicted in Figure 4. Using the system gain g, the output power by system can be written as:

$$P = g\left[4R_a kT \left(\frac{R_r}{R_a+R_r}\right)^2 + I_{noise}^2 \left(\frac{R_a R_r}{R_a+R_r}\right)^2 + E_{noise}^2\right]. \tag{4}$$

In this equation, the noise from the subsequent stages can be treated as a constant referred to the input, and it is incorporated into E_{noise}^2.

Some of these parameters, such as E_{noise} and I_{noise} are unknown, but these can be determined by a calibration procedure. The amplifier input port is connected to a selected resistor load, and then short-circuit for calibration measurement. By leveraging the known gain, both the current noise and voltage noise can be accurately determined over the working frequency range by solving Equation (4) [35]. A more accurate calibration method suitable for high frequency is proposed in Section 4.

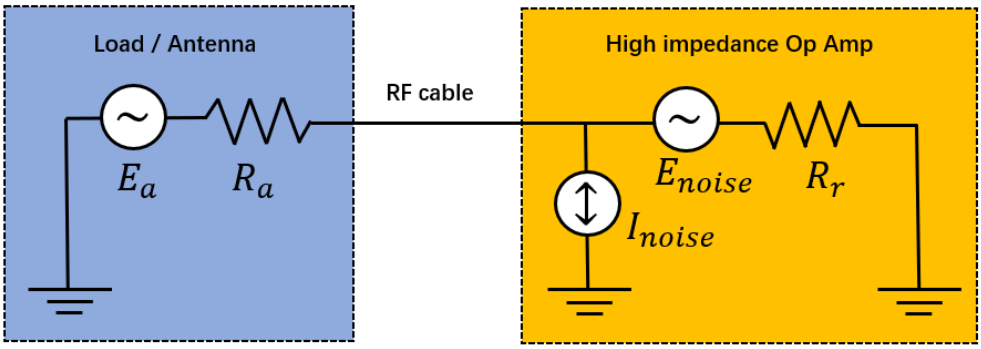

Figure 4. Simplified signal model of operational amplifier. The total noise of the amplifier is modeled as a current source and a voltage source, with the signal from the antenna considered separately.

3. SIGNAL AND NOISE MODEL AT HIGH FREQUENCY

The 21-cm global spectrum experiment utilizing a high-impedance operational amplifier has the potential to cover the entire bandwidth of interest, such as the range from 30 MHz to 200 MHz. At frequencies exceeding a few Megahertz, propagation effects and reflections will induce changes in the signal, which were not accounted for in the classical model Equation (4). Here, we employ a two-port network representation, a standard tool in microwave engineering, to characterize signal propagation effects, as illustrated in Figure 5.

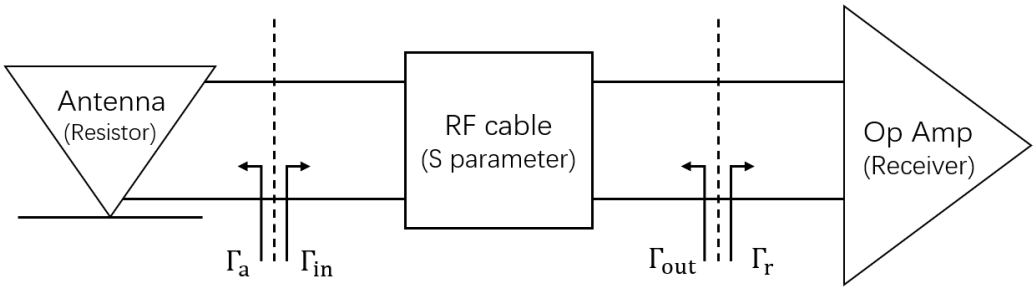

Figure 5. The two-port network diagram of the high-impedance operational amplifier is shown, with the antenna as the source, the receiver as the load, and the RF cable between them represented as a two-port network. The reflection coefficient Γ is distinguished by subscripts, and the arrow indicates the direction of the reflected wave.

In this model, the RF cable between the antenna and the amplifier is treated as a two-port network, while the antenna and operational amplifier connected to the two ports. Γ_a denotes the antenna reflection coefficient, Γ_r denotes the receiver reflection coefficient, Γ_{in} denotes the reflection coefficient observed from port 1 (left port in Fig.5) toward the receiver, and Γ_{out} denotes the reflection coefficient observed from port 2 (right port in Fig.5) toward the antenna. The RF cable between the antenna and receiver is characterized by an S-parameter matrix. All reflection coefficients and S-parameters can be measured directly by using a vector network analyzer (VNA). Impedance mismatches at the ports give rise to multiple reflections, while inherent cable losses introduce additional noise through power dissipation.

The transmitted signal at the network output can then be expressed as:

$$\langle E_a^2 \rangle = (4R_a kT + \langle |V_{amb}|^2 \rangle)|S_0|^2. \tag{5}$$

The first term in the parentheses corresponds to the sky signal received by the antenna, where T denotes the antenna temperature. The second term, $|V_{amb}|^2$, represents the noise contribution from RF cable losses, which is equivalently referred to the input component of port 1. S_0 represents the voltage propagation factor from the antenna to the receiver.

We first consider the term $|V_{amb}|^2$, whose general expression is given by:

$$\langle |V_{amb}|^2 \rangle = 4Z_0 kT_{amb} \frac{(1-|\Gamma_a|^2)}{|1-\Gamma_a|^2} \left(\frac{1-G_{21}}{G_{21}} \right), \tag{6}$$

where Z_0 is the characteristic impedance of the transmission line ($50\,\Omega$), T_{amb} denotes the ambient temperature of the RF cable, and G_{21} represents the available power gain from port 1 to port 2 of the two-port network:

$$G_{21} = \frac{|S_{21}|^2(1-|\Gamma_a|^2)}{|1-S_{11}\Gamma_a|^2(1-|\Gamma_{out}|^2)}, \tag{7}$$

S_{11} and S_{21} are the S-parameters of the RF cable. The voltage propagation factor, S_0, which relates the voltage at port 1 to that at port 2, is subsequently derived as:

$$S_0 = \frac{1-\Gamma_a}{2} \frac{S_{21}(1+\Gamma_r)}{(1-S_{22}\Gamma_r)(1-\Gamma_a\Gamma_{in})}, \tag{8}$$

the detailed derivations of S_0 are given in the Appendix.

We now turn our attention to the amplifier noise. We can also model the internal noise of the operational amplifier by using a voltage source and a current source, in a form similar to that in Equation (4), but with modifications to account for the parasitic effects of the resistor at high frequencies. In addition to the current and voltage noise terms, another critical contribution to the noise is the correlation between the voltage and current noises. In essence, the correlation originates from the amplifier itself, largely independent of the thermal noise from peripheral circuits. The correlation term is generally of the form $C_1R_p + C_2X_p$, and the complex correlation coefficient is defined as $C = C_1 + iC_2$, with R_p and X_p the real and imaginary parts of Z_p, respectively, which represents the parallel combination of the output impedance Z_{out} and the receiver input impedance Z_r. This is often overlooked, as it does not dominate the noise, but in a high precision analysis it must be taken into account. This correlation between the noise current and voltage can be measured by employing various calibration sources and feedback resistors [38], and the calibration procedure has been further streamlined through cascading and parallel connection of multiple amplifiers [39].

Due to parasitic effects at high frequencies, both the magnitude and phase of the reflection coefficients for the resistors vary with frequency. Therefore, each resistor must be treated as an impedance during calibration, a consideration fully incorporated into our model. However, when calculating the thermal noise of resistors or the antenna temperature, since the reactive part does not generate thermal noise, the resistance value should be used. Consequently, considering the parasitic capacitance and inductance inherent in the resistors, we derive the total noise as follows:

$$\langle E_t^2 \rangle = \langle {I_{noise}}^2 \rangle |Z_p|^2 + \langle E_{noise}^2 \rangle + (C_1R_p + C_2X_p). \tag{9}$$

Drawing from Equation (4) and the theoretical framework established herein, the total power received by the system can be written as:

$$P = g\left[\left(4R_a kT + \langle |V_{amb}|^2 \rangle\right) |S_0|^2 + \langle I_{noise}^2 \rangle |Z_p|^2 + \langle E_{noise}^2 \rangle + (C_1R_p + C_2X_p) \right]. \tag{10}$$

We examine a specific scenario where the antenna temperature is equal to the ambient temperature. In this case, when viewed from Port 2 toward the source, the antenna and RF cable can naturally be treated as a unified system. Consequently, the received signal degrades to a form that resembles that of Equation (4):

$$\langle {E_a}^2 \rangle = 4R_{out} kT \left| \frac{Z_r}{Z_{out} + Z_r} \right|^2, \tag{11}$$

where R_{out} denotes the real part of the output impedance Z_{out}, which can be derived from the reflection coefficient Γ_{out}. This equation yields results consistent with Equation (5), thus offering a means to cross-check the validity of our model. However, the two-port network model enables a more accurate analysis of transmission losses. We note that the reflection coefficient of the operational amplifier Γ_r is typically very close to 1. In this anomalous conditions, with measurement error, the measured reflection coefficient may exceed 1, resulting in a negative Z_r. Under these conditions, the classical voltage divider model in Equation (11) becomes invalid or inaccurate, but the S_0 formulation in Equation (8) still accurately describes signal propagation. The RF cable losses and multiple reflections due to extreme mismatch render the traditional voltage divider model increasingly unsuitable at high frequencies and and can only serve as a simple approximation in certain specific scenarios.

4. MULTI-RESISTANCE CALIBRATION

As the receiver introduces additional noise and gain variations, it is essential to design a calibration scheme based on the signal model to accurately recover the true antenna temperature. Equation (10) contains five unknown system parameters: the gain g, the noise voltage E_{noise}, the noise current I_{noise}, and the correlation coefficients C_1 and C_2. Since these parameters exhibit temporal variations, the calibration must be carried out frequently during the measurement process.

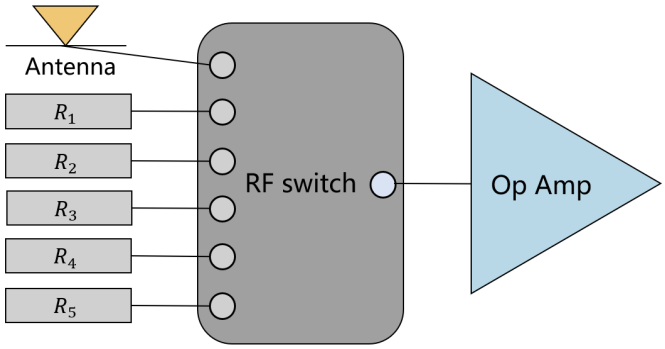

Figure 6. Diagram of the multi-resistance calibration system. The system comprises a RF switch and five known resistors connected to its ports. In the high-impedance receiver, the antenna is also connected to one port of the switch, which then connects to the input of the operational amplifier. During calibration, the RF switch sequentially selects each port, using the signals from the five known resistors to calculate all system parameters, and then employing the antenna signal to recover the true antenna temperature.

We have designed the multi-resistance calibration for the high-impedance system, with the schematic shown in Figure 6. As the RF switch alternates between various calibration resistors and the antenna, equations containing the five unknown system parameters are constructed from the measured physical temperature and signal of each resistor based on Equation (10). For the five calibration resistors, the set of equations after one switching cycle is given by

$$\begin{cases} P_{(R_1)} = g\left[\left(4R_1kT_{(R_1)} + \langle|V_{amb(R_1)}|^2\rangle\right)|S_{0(R_1)}|^2 + \langle I_{noise}^2\rangle|Z_{p(R_1)}|^2 + \langle E_{noise}^2\rangle + (C_1R_{p(R_1)} + C_2X_{p(R_1)})\right], \\ P_{(R_2)} = g\left[\left(4R_2kT_{(R_2)} + \langle|V_{amb(R_2)}|^2\rangle\right)|S_{0(R_2)}|^2 + \langle I_{noise}^2\rangle|Z_{p(R_2)}|^2 + \langle E_{noise}^2\rangle + (C_1R_{p(R_2)} + C_2X_{p(R_2)})\right], \\ P_{(R_3)} = g\left[\left(4R_3kT_{(R_3)} + \langle|V_{amb(R_3)}|^2\rangle\right)|S_{0(R_3)}|^2 + \langle I_{noise}^2\rangle|Z_{p(R_3)}|^2 + \langle E_{noise}^2\rangle + (C_1R_{p(R_3)} + C_2X_{p(R_3)})\right], \\ P_{(R_4)} = g\left[\left(4R_4kT_{(R_4)} + \langle|V_{amb(R_4)}|^2\rangle\right)|S_{0(R_4)}|^2 + \langle I_{noise}^2\rangle|Z_{p(R_4)}|^2 + \langle E_{noise}^2\rangle + (C_1R_{p(R_4)} + C_2X_{p(R_4)})\right], \\ P_{(R_5)} = g\left[\left(4R_5kT_{(R_5)} + \langle|V_{amb(R_5)}|^2\rangle\right)|S_{0(R_5)}|^2 + \langle I_{noise}^2\rangle|Z_{p(R_5)}|^2 + \langle E_{noise}^2\rangle + (C_1R_{p(R_5)} + C_2X_{p(R_5)})\right]. \end{cases} \tag{12}$$

Here, the subscript R_n denotes the corresponding quantity when the switch is connected to the resistor R_n. The quantities $\langle|V_{amb(R_n)}|^2\rangle$, $|S_{0(R_n)}|^2$, $|Z_{p(R_n)}|^2$, $R_{p(R_n)}$ and $X_{p(R_n)}$ can be derived from the VNA measurement results using the aforementioned equations. By simultaneously solving the equations corresponding to the five calibration resistors, all five unknown parameters can then be solved.

Once the system parameters are determined, Equation (10) is reapplied to the antenna signal to accurately recover the antenna temperature:

$$T_{ant} = \frac{P - \Delta P}{4R_akg|S_0|^2}. \tag{13}$$

Where T_{ant} represents the antenna temperature, P denotes the system output power when the RF switch is connected to the antenna, while ΔP represents the power contribution from the system effects:

$$\Delta P = g[\langle|V_{amb}|^2\rangle)|S_0|^2 + \langle I_{noise}^2\rangle|Z_p|^2 + \langle E_{noise}^2\rangle + (C_1R_p + C_2X_p)]. \tag{14}$$

It should be noted that since this method switches only the calibration source without modifying the amplifier circuit, the simplified model described in the previous sections remains valid because certain noise components are

merged into a function that depends solely on the source. In addition, the validity of this calibration scheme hinges on the five system parameters remaining constant across equations derived from different calibration sources. Since these parameters vary with temperature and voltage, temperature control and power regulation are implemented in the receiver to ensure their stability during each switching cycle.

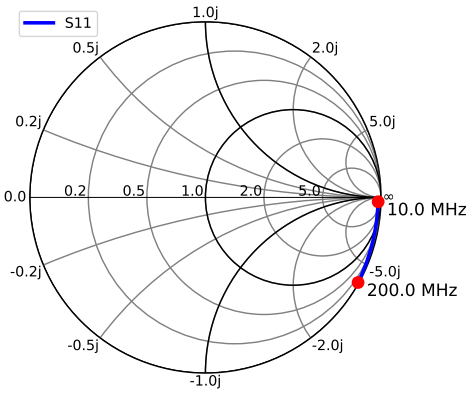

Figure 7. Smith Chart showing the reflection coefficient of high-impedance operational amplifier.The blue line indicates that rotates counterclockwise with increasing frequency on the chart, where the red dots mark 10 MHz and 200 MHz.

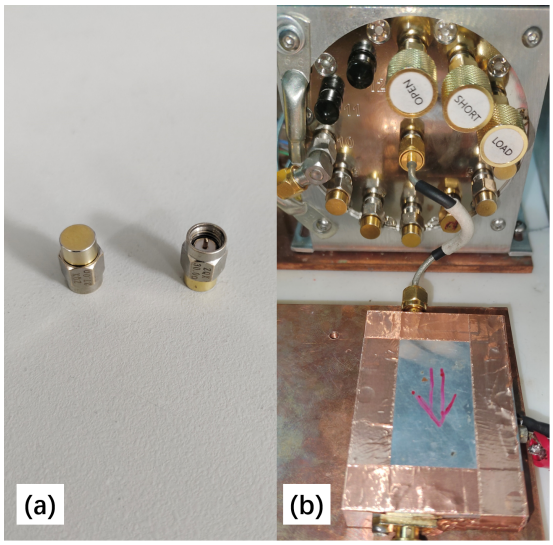

Figure 8. Photograph of the calibration system: (a) shows the resistors used for calibration, and (b) illustrates the calibration setup, where the resistors are installed on the RF switch, with the output connected to the operational amplifier via an RF cable.

The multi-resistance calibration method is highly efficient as it necessitates only a few resistors as calibration sources, substantially simplifying the calibration process. Compared to the traditional Y-factor method, this calibration approach does not require a large temperature difference between the different sources. Instead, it only requires the collection of temperature data from the calibration resistors and the ambient temperature for calculating RF cable loss.

The physical temperatures of the resistors are measured using platinum resistance temperature detector (RTD) PT1000 sensors connected to a high-performance DAQ (Data Acquisition system). The PT1000 has a resistance of 1000Ω at 0 °C, and its resistance varies with temperature according to the Callendar–Van Dusen(CVD) equation [40; 41; 42]. The DAQ, model LABJACK U6 Pro [1], integrates a 24-bit low-noise ADC that converts analog voltage signals into digital data, which is then transmitted to a computer via USB. During measurement, the DAQ measures the voltage across the sensor using a voltage divider circuit, calculates the sensor's resistance, and determines the temperature based on temperature-resistance CVD relationship.

[1] https://support.labjack.com/docs/u6-datasheet

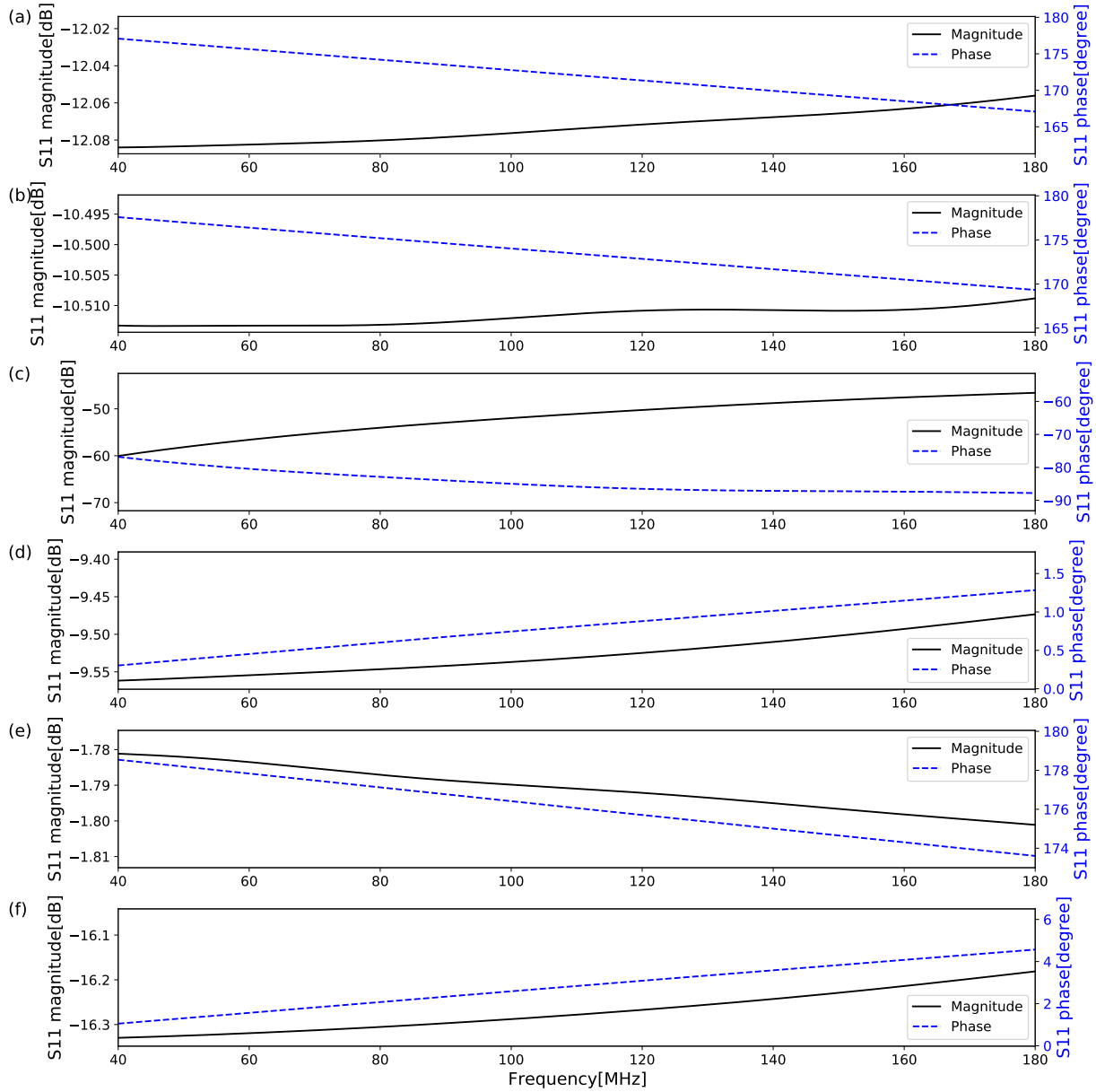

Figure 9. The S_{11} parameters of sources in the calibration are shown in the figure. From top to bottom, (a)-(f) are R_a , R_1, R_2, R_3, R_4, R_5 respectively. The solid black line represents the magnitude, and the dashed blue line represents the phase. In each subfigure, the horizontal axis represents frequency in MHz, the left vertical axis denotes the magnitude of S_{11} in dB, and the right vertical axis represents the phase of S_{11} in degrees.

For the operational amplifier of our experiment, we used a Texas Instruments OPA855 [2] , which features an exceptionally wide 8 GHz Gain-Bandwidth Product and a Common Mode Rejection Ratio (CMRR) of approximately 60 dB. It is powered by 5V supply, and the Power Supply Rejection Ratio (PSRR) is about 40 dB. In the circuit setup, the amplifier gain is set to approximately 16 dB, and a 6.2 kΩ resistor is used as the input parallel resistance, which provides an optimal balance between minimizing noise contributions and ensuring sufficient voltage division at the amplifier input. The Smith chart of the amplifier's reflection coefficient, measured by a VNA, is shown in Figure 7.

[2] https://www.ti.com/product/OPA855

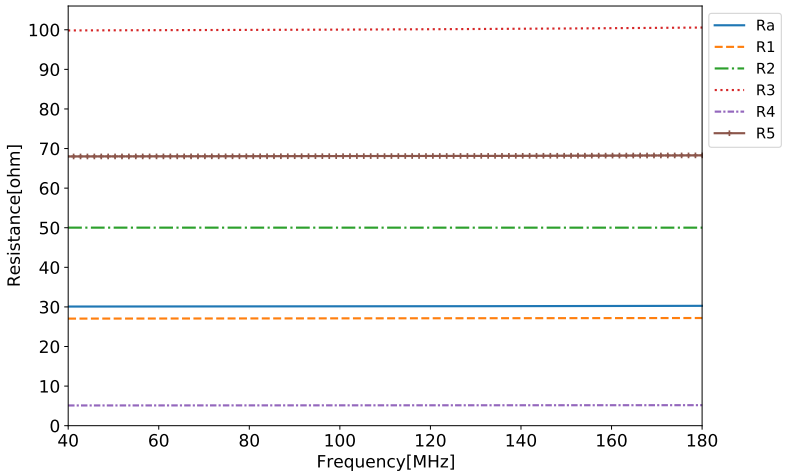

Figure 10. Antenna substitute resistor R_a and calibration resistances R_1, R_2, R_3, R_4, R_5 as a function of frequency. Different resistors are indicated by distinct lines as shown in the legend. All these resistance values are calculated from the reflection coefficients measured by VNA.

Over the frequency range of 10 MHz to 200 MHz, the input impedance of the amplifier is significantly higher than 50 Ω, causing the reflection coefficient to approximate an open-circuit condition. By applying the voltage divider principle, the operational amplifier captures most of the signal due to its high input impedance.

The resistors used for calibration should have widely different values, to avoid degeneracy in the measurement equations. However, resistance values that are either much higher or much lower than the characteristic impedance of the cable may introduce instability risks. Furthermore, as the mismatch increases, stronger standing waves are formed within the circuit, making spectrum reconstruction more challenging. We carefully selected resistor values that strike a balance between these two requirements, including values both above and below the characteristic impedance of 50 Ω. A 30 Ω resistor, deviating from the characteristic impedance, is used as an antenna substitute in the laboratory, which helps validate the general applicability of the calibration method. Table 1 summarizes the selection of all resistance values used in the calibration experiment.

Table 1. List of calibration resistors and antenna substitute resistor.

Resistor	R_a	R_1	R_2	R_3	R_4	R_5
Value	30Ω	5.1Ω	27Ω	50Ω	68Ω	100Ω

Figure 8 shows the calibration resistors used in the experiment, along with their installation configuration. The custom resistors with SMA male connectors are directly connected to the ports of the RF switch, and the switch output is linked to the operational amplifier input via a short RF cable.

The reflection coefficients of the antenna R_a and the calibration resistors, measured by the VNA, are shown in Figure 9. The resistance values of the calibration resistors, calculated from the reflection coefficient using $R = \mathrm{Re}(Z_0 \frac{1+\Gamma}{1-\Gamma})$, are illustrated in Figure 10. The figure clearly identifies the resistance values of the selected resistors and accurately depicts the true high-frequency resistance values of them, as these values are derived from VNA-measured reflection coefficients that inherently account for all high-frequency parasitic effects of the resistors.

5. CALIBRATION RESULTS

To validate the multi-resistance calibration, we carried out experiments using a high-impedance receiver system designed for the global spectrum measurement. The analog frontend includes the calibration system, amplifier chain, and temperature control system, while the digital backend integrates a digital acquisition board, temperature acquisition

DAQ, the vector network analyzer, and an X86-based microcomputer. During the global spectrum experiment in the field, the input of the analog frontend was connected to a monopole antenna. The signal was amplified by the analog frontend and then digitized at the digital backend. In the laboratory validation, a resistor with known resistance was used as a substitute for the antenna.

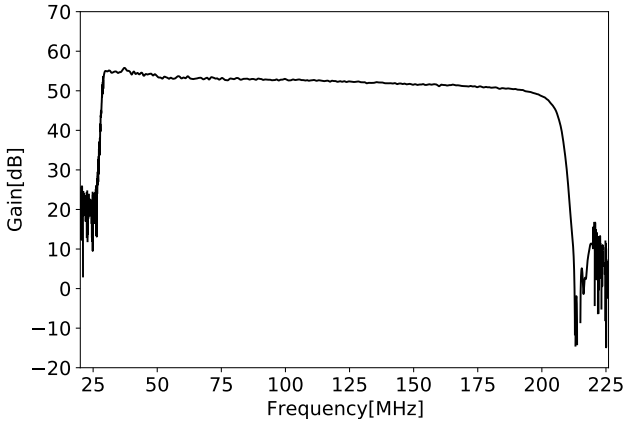

Figure 11. System gain obtained through multi-resistance calibration.

Figure 11 shows the system gain g determined through calibration, which is approximately 53 dB within the band, while the RF filter attenuates frequencies below 30 MHz and above 200 MHz. Since the operational amplifier's gain

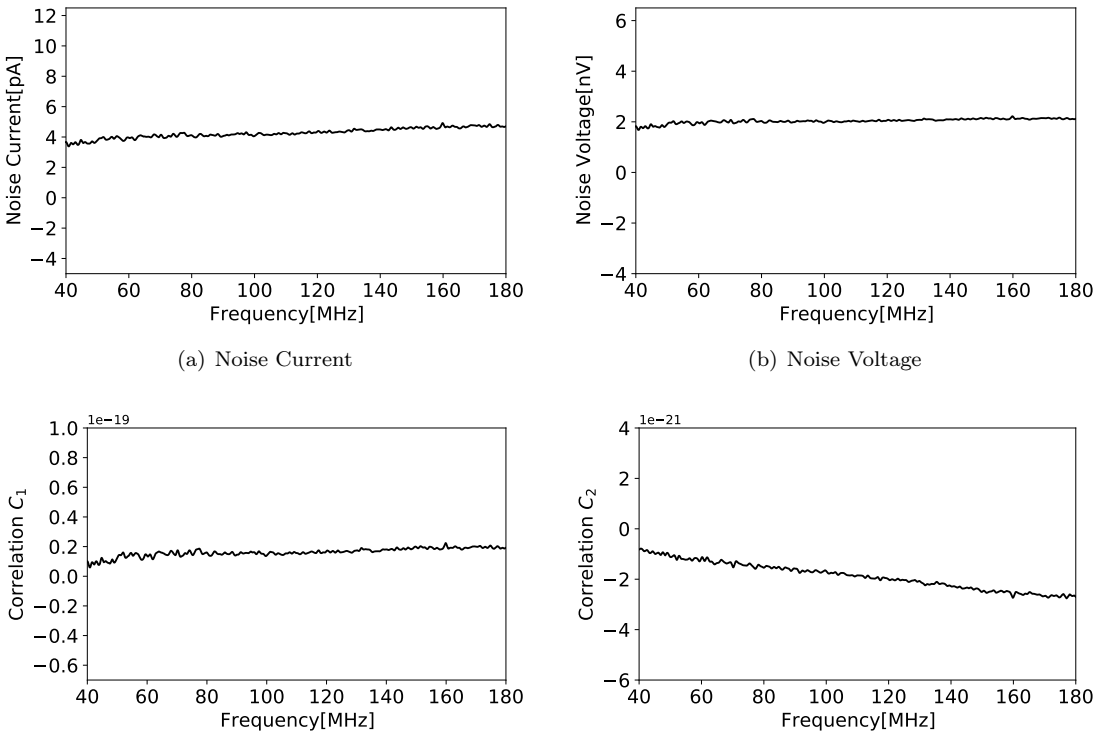

(a) Noise Current

(b) Noise Voltage

(c) Correlation Term 1

(d) Correlation Term 2

Figure 12. Calibration result of our operational amplifier noise model parameters. (a) The noise current (b) The noise voltage. (c) C_1. (d) C_2.

depends solely on the ratio of R_f to R_g, the system gain remains smooth across the observation band, ensuring a consistent response that is beneficial for extracting 21-cm signals in global spectrum experiments.

The frequency-dependent noise parameters after calibration are shown in Figure 12. Sub-figure (a) shows that the noise current is around 4 pA/$\sqrt{\text{Hz}}$. The noise current originates partly from the operational amplifier itself and partly from the equivalent thermal noise current of the resistor in parallel with the non-inverting input. When recovering the true sky temperature, only the total noise current needs to be considered, simplifying the calibration process. It is important to note that since the sources of these two noise currents are independent, their noise can be directly summed without any correlation terms. Thus, by subtracting the equivalent thermal noise current, the internal noise current of the amplifier is determined to be approximately 2.5 pA/$\sqrt{\text{Hz}}$, which is consistent with the data sheet value.

The overall noise voltage obtained through calibration is shown in sub-figure (b), with a magnitude of approximately 2 nV/$\sqrt{\text{Hz}}$, which also dominates the amplifier noise. Similar to current noise, the voltage noise consists of the amplifier's inherent voltage noise, thermal noise from the circuitry, and noise from subsequent amplification stages. The first two components contribute significantly, while the noise from the subsequent stages constitutes a minor portion. Assuming the inverting and non-inverting currents are equal (as in Figure 3), the noise contribution from the inverting side can be estimated. Subtracting this from the total voltage noise yields an inherent noise voltage of approximately 1 nV/$\sqrt{\text{Hz}}$, consistent with the datasheet value. The correlation terms arise between the amplifier's internal noise current and voltage noise, with this correlation mathematically originating from the cross terms during their summation.Using the multi-resistance calibration presented in this paper, the real and imaginary parts of these cross terms can be directly calculated without the need to compute the specific values of the internal noise current and voltage noise separately. The calibration results of the correlation terms are presented in sub-figures (c) and (d), with the real part C_1 having a positive value and the imaginary part C_2 having a negative value, respectively.

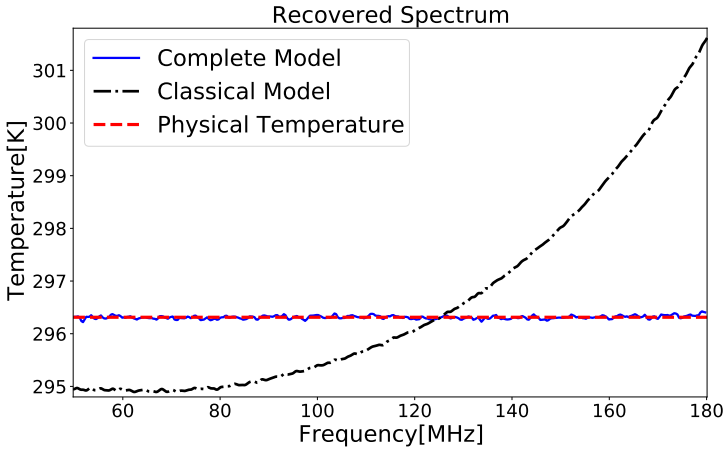

Figure 13. Result of calibrated 30Ω spectrum use Multi-resistances calculation shown with blue solid line, the red dash line is physical temperature of the resistor. By contrast, the dashed-dotted line shows the calibrated spectrum based on the classical model.

By utilizing the received antenna signals and the calibrated system parameters, the antenna temperature can be recovered using Equation (10). In the laboratory, since a resistor is used as a substitute for the antenna, the antenna temperature is expected to be physical temperature of the resistor. Figure 13 depicts the recovered antenna temperature spectrum result as a black line, and the physical temperature of the resistor represented by a dashed line. As shown in the figure, the calibrated antenna temperature exhibits no obvious structure and remains constant with frequency. This indicates that the calibration effectively removes the propagation effects and system noise, ensuring accurate recovery of the antenna temperature across frequencies. The RMS standard deviation on the temperature structure from 50 MHz to 180 MHz is calculated to be 31.19 mK, basically satisfying the need for the present 21cm global spectrum experiment. As a comparison, we also use the classical operational amplifier model in Equation (4) to retrieve the temperature spectrum. This spectrum, shown by the dashed-dotted line, exhibits an error of several Kelvin. As a

result, it is evident that by accounting for high-frequency propagation and correlated noise, the model proposed in this paper achieves an accuracy improvement exceeding two orders of magnitude compared with the classical model.

6. CONCLUSION

In the past decade, global spectrum experiments have become a more accessible approach for exploring the early history of the universe. It only requires a single antenna to continuously observe the sky as earth rotates, extracting the early 21-cm spectrum from the sky-averaged signal. By analyzing the structures on these 21-cm spectrum, the early universe's evolution can be inferred. Currently, conventional matching receivers for this experiment typically achieve only a one-octave wideband measurement. We propose a high-impedance receiver scheme that uses an operational amplifier as the first stage, which can overcome the bandwidth limitations caused by impedance matching. Since the high frequency degrades the accuracy of the classical model, it is necessary to reanalyze the transmission model for this system.

This paper simplifies the classical operational amplifier signal model and develops a comprehensive model for higher frequencies and greater accuracy. Based on this signal model, a multi-resistance calibration method is proposed to calibrate system parameters and antenna temperatures in real-time. In the laboratory, resistors are used as substitutes for antennas to test the calibration effect, achieving a calibration accuracy of approximately 30 mK, indicating the system's capability for 21-cm global spectrum observation. Furthermore, the multi-resistance calibration method presents a novel solution for high-frequency, high-precision spectral measurements, potentially opening new research avenues in radio frequency communications and precision metrology. Currently, a field experiment is underway near the site of Tianlai Array [43; 44]. The observation data will be further processed and is expected to extract the 21-cm signal in the near future.

ACKNOWLEDGEMENT

We thank Jixia Li, Jiajun Yuan, Juyong Zhang, Yougang Wang, Yidong Xu, Bin Yue, Shifan Zuo who helped with various aspects on the work. This work is supported by the Chinese Academy of Science Instrument R&D program grant ZDKYYQ20200008, the NSFC grants 12361141814, 12273070, 12473094, 12203061, 12303004, 11973047, the NKPs grants 2022YFF0504300, 2022YFF0503404 and by the Specialized Research Fund for State Key Laboratory of Radio Astronomy and Technology.

APPENDIX

We present here the derivation of Equation 8 for propagation factor method using two-port network. For a two-port network, the transducer power gain G_T characterizing the signal amplification from port 1 to port 2 can be written as

$$G_T = \frac{P_L}{P_{avs}} = \frac{|S_{21}|^2\left(1-|\Gamma_S|^2\right)\left(1-|\Gamma_L|^2\right)}{|1-\Gamma_S\Gamma_{\rm in}|^2|1-S_{22}\Gamma_L|^2}, \tag{A.1}$$

here Γ_S represents the reflection coefficient of the source, with Γ_L being the reflection coefficient of the load. P_{avs} represents the available power of the source

$$P_{avs} = \frac{|V_S|^2}{8Z_0}\frac{|1-\Gamma_S|^2}{1-|\Gamma_S|^2}. \tag{A.2}$$

Accordingly, the power at the load can be expressed as

$$P_L = G_T * P_{avs} = \frac{|V_S|^2|1-\Gamma_S|^2}{8Z_0}\frac{|S_{21}|^2\left(1-|\Gamma_L|^2\right)}{|1-S_{22}\Gamma_L|^2|1-\Gamma_S\Gamma_{in}|^2}. \tag{A.3}$$

Moreover, this power can also be denoted by the voltage at the operational amplifier position on the transmission line

$$P_L = \frac{|V_o^+|^2}{2Z_0}\left(1-|\Gamma_L|^2\right). \tag{A.4}$$

The total voltage at the source's port is

$$|V(0)|^2 = |V_o^+|^2 |\,(1+\Gamma_L)\,|^2 = \frac{|V_S|^2|1-\Gamma_S|^2}{4}\frac{|S_{21}|^2|1+\Gamma_L|^2}{|1-S_{22}\Gamma_L|^2|1-\Gamma_S\Gamma_{in}|^2}. \tag{A.5}$$

Within our system, the source is the antenna and the load is the operational amplifier. Substituting these parameters into the formula results in the expression for the propagation coefficient S_0.

Consider a two-port network at T_{amb}. If input noise $N1 = KT_{amb}B$ is added to port 1, the available noise power at port 2 is

$$N_2 = G_{21}KTB + G_{21}N_{added}, \tag{A.6}$$

where N_{added} stands for the noise produced by the network, and we equivalently place this noise at port 1. Due to thermodynamic equilibrium, the available output noise power has to be

$$N_2 = kT_{amb}B. \tag{A.7}$$

Therefore, the available noise power supplied by the two-port network can be derived.

$$N_{added} = \frac{1-G_{21}}{G_{21}}kTB, \tag{A.8}$$

where G_{21} is the available power gain from port 1 to port 2, and its expression is given by Equation 7. Since N_{added} is an available power, it can also be written in the form of Equation A.2.

$$N_{added} = \frac{|V_{amb}|^2}{4Z_0}\frac{|1-\Gamma_S|^2}{1-|\Gamma_S|^2}, \tag{A.9}$$

where $|V_{amb}|$ is the root mean square (RMS) of the two-port noise voltage. Compared with Equation A.2, there is no need to consider the time average of the voltage again, so the coefficient of the denominator here is 4. By combining these equations, the mean square value of the noise voltage introduced by the two-port network (given by Equation 6) is obtained, which is exactly the noise introduced by the RF cable loss in the system.

REFERENCES

[1]Miguel F. Morales and J. Stuart B. Wyithe. Reionization and cosmology with 21-cm fluctuations. *Annual Review of Astronomy and Astrophysics*, 48(Volume 48, 2010):127–171, 2010.

[2]Jonathan R Pritchard and Abraham Loeb. 21 cm cosmology in the 21st century. *Reports on Progress in Physics*, 75(8):086901, 2012.

[3]Peter E Dewdney, Peter J Hall, Richard T Schilizzi, and T Joseph LW Lazio. The square kilometre array. *Proceedings of the IEEE*, 97(8):1482–1496, 2009.

[4]David R DeBoer, Aaron R Parsons, James E Aguirre, Paul Alexander, Zaki S Ali, Adam P Beardsley, Gianni Bernardi, Judd D Bowman, Richard F Bradley, Chris L Carilli, et al. Hydrogen epoch of reionization array (hera). *Publications of the Astronomical Society of the Pacific*, 129(974):045001, 2017.

[5]Michael P van Haarlem, Michael W Wise, AW Gunst, George Heald, John P McKean, Jason WT Hessels, A Ger de Bruyn, Ronald Nijboer, John Swinbank, Richard Fallows, et al. Lofar: The low-frequency array. *Astronomy & astrophysics*, 556:A2, 2013.

[6]Steven John Tingay, Robert Goeke, Judd D Bowman, David Emrich, Stephen M Ord, Daniel A Mitchell, Miguel F Morales, Tom Booler, Brian Crosse, Randall B Wayth, et al. The murchison widefield array: The square kilometre array precursor at low radio frequencies. *Publications of the Astronomical Society of Australia*, 30, 2013.

[7]Gregory Paciga, Joshua G. Albert, Kevin Bandura, Tzu-Ching Chang, Yashwant Gupta, Christopher Hirata, Julia Odegova, Ue-Li Pen, Jeffrey B. Peterson, Jayanta Roy, J. Richard Shaw, Kris Sigurdson, and Tabitha Voytek. A simulation-calibrated limit on the hi power spectrum from the gmrt epoch of reionization experiment. *Monthly Notices of the Royal Astronomical Society*, 433(1):639–647, 05 2013.

[8]Yan Huang, Xiang-Ping Wu, Qian Zheng, Jun-Hua Gu, and Haiguang Xu. The radio environment of the 21 centimeter array: Rfi detection and mitigation. *Research in Astronomy and Astrophysics*, 16(2):016, feb 2016.

[9]Jonathan R Pritchard and Abraham Loeb. Evolution of the 21 cm signal throughout cosmic history. *Physical Review D—Particles, Fields, Gravitation, and Cosmology*, 78(10):103511, 2008.

[10]Xuelei Chen and Jordi Miralda-Escudé. The spin-kinetic temperature coupling and the heating rate due to lyα scattering before reionization: predictions for 21 centimeter emission and absorption. *The Astrophysical Journal*, 602(1):1, 2004.

[11]Aviad Cohen, Anastasia Fialkov, and Rennan Barkana. Charting the parameter space of the 21-cm power spectrum. *Monthly Notices of the Royal Astronomical Society*, 478(2):2193–2217, 2018.

[12]Bohdan Novosyadlyj, Yurii Kulinich, Gennadi Milinevsky, and Valerii Shulga. Formation of the hydrogen line 21-cm in dark ages and cosmic dawn: dependences on cosmology and first light. *Monthly Notices of the Royal Astronomical Society*, 526(2):2724–2735, 2023.

[13]Rajesh Mondal, Rennan Barkana, and Anastasia Fialkov. Constraining exotic dark matter models with the dark ages 21-cm signal. *Monthly Notices of the Royal Astronomical Society*, 527(1):1461–1471, 2024.

[14]Judd D Bowman, Alan EE Rogers, Raul A Monsalve, Thomas J Mozdzen, and Nivedita Mahesh. An absorption profile centred at 78 megahertz in the sky-averaged spectrum. *Nature*, 555(7694):67–70, 2018.

[15]Saurabh Singh, Ravi Subrahmanyan, N Udaya Shankar, Mayuri Sathyanarayana Rao, Anastasia Fialkov, Aviad Cohen, Rennan Barkana, BS Girish, A Raghunathan, R Somashekar, et al. Saras 2 constraints on global 21 cm signals from the epoch of reionization. *The Astrophysical Journal*, 858(1):54, 2018.

[16]Tabitha C Voytek, Aravind Natarajan, Jose Miguel Jáuregui García, Jeffrey B Peterson, and Omar López-Cruz. Probing the dark ages at z 20: The sci-hi 21 cm all-sky spectrum experiment. *The Astrophysical Journal Letters*, 782(1):L9, 2014.

[17]L Philip, Z Abdurashidova, HC Chiang, N Ghazi, A Gumba, HM Heilgendorff, JM Jáuregui-García, K Malepe, CD Nunhokee, J Peterson, et al. Probing radio intensity at high-z from marion: 2017 instrument. *Journal of Astronomical Instrumentation*, 8(02):1950004, 2019.

[18]D C Price, L J Greenhill, A Fialkov, G Bernardi, H Garsden, B R Barsdell, J Kocz, M M Anderson, S A Bourke, J Craig, M R Dexter, J Dowell, M W Eastwood, T Eftekhari, S W Ellingson, G Hallinan, J M Hartman, R Kimberk, T Joseph W Lazio, S Leiker, D MacMahon, R Monroe, F Schinzel, G B Taylor, E Tong, D Werthimer, and D P Woody. Design and characterization of the large-aperture experiment to detect the dark age (leda) radiometer systems. *Monthly Notices of the Royal Astronomical Society*, 478(3):4193–4213, 05 2018.

[19]Eloy de Lera Acedo. Reach: Radio experiment for the analysis of cosmic hydrogen. In *2019 International Conference on Electromagnetics in Advanced Applications (ICEAA)*, pages 0626–0629, 2019.

[20]E de Lera Acedo, DIL de Villiers, N Razavi-Ghods, W Handley, A Fialkov, A Magro, D Anstey, HTJ Bevins, R Chiello, J Cumner, et al. The reach radiometer for detecting the 21-cm hydrogen signal from redshift z 7.5–28. *Nature Astronomy*, 6(8):984–998, 2022.

[21]Marcin Sokolowski, Steven E Tremblay, Randall B Wayth, Steven J Tingay, Nathan Clarke, Paul Roberts, Mark Waterson, Ronald D Ekers, Peter Hall, Morgan Lewis, et al. Bighorns-broadband instrument for global hydrogen reionisation signal. *Publications of the Astronomical Society of Australia*, 32, 2015.

[22]DC Price, LJ Greenhill, Anastasia Fialkov, G Bernardi, H Garsden, BR Barsdell, J Kocz, MM Anderson, SA Bourke, J Craig, et al. Design and characterization of the large-aperture experiment to detect the dark age (leda) radiometer systems. *Monthly Notices of the Royal Astronomical Society*, 478(3):4193–4213, 2018.

[23]Bang D. Nhan, David D. Bordenave, Richard F. Bradley, Jack O. Burns, Keith Tauscher, David Rapetti, and Patricia J. Klima. Assessment of the projection-induced polarimetry technique for constraining the foreground spectrum in global 21 cm cosmology. *The Astrophysical Journal*, 883(2):126, Sep 2019.

[24]R. A. Monsalve, C. Altamirano, V. Bidula, R. Bustos, C. H. Bye, H. C. Chiang, M. Díaz, B. Fernández, X. Guo, I. Hendricksen, E. Hornecker, F. Lucero, H. Mani, F. McGee, F. P. Mena, M. Pessôa, G. Prabhakar, O. Restrepo, J. L. Sievers, and N. Thyagarajan. Mapper of the IGM spin temperature: instrument overview. *MNRAS*, 530(4):4125–4147, June 2024.

[25]Xuelei Chen, Jingye Yan, Li Deng, Fengquan Wu, Lin Wu, Yidong Xu, and Li Zhou. Discovering the sky at the longest wavelengths with a lunar orbit array. *Philosophical Transactions of the Royal Society A*, 379(2188):20190566, 2021.

[26]Xuelei Chen, Jingye Yan, Yidong Xu, Li Deng, Fengquan Wu, Lin Wu, Li Zhou, Xiaofeng Zhang, Xiaocheng Zhu, Zhongguang Yang, and Ji Wu. Discovering the sky at the longest wavelength missiona pathfinder for exploring the cosmic dark ages. *Chinese Journal of Space Science*, 43(1):43, 2023.

[27]Yuan Shi, Furen Deng, Yidong Xu, Fengquan Wu, Qisen Yan, and Xuelei Chen. Lunar orbit measurement of the cosmic dawn's 21 cm global spectrum. *The Astrophysical Journal*, 929(1):32, 2022.

[28]Jack O. Burns, J. Lazio, S. Bale, J. Bowman, R. Bradley, C. Carilli, S. Furlanetto, G. Harker, A. Loeb, and J. Pritchard. Probing the first stars and black holes in the early universe with the dark ages radio explorer (dare). *Advances in Space Research*, 49(3):433–450, 2012.

[29]Jack Burns, Stuart Bale, Richard Bradley, Z Ahmed, SW Allen, J Bowman, S Furlanetto, R MacDowall, J Mirocha, B Nhan, et al. Global 21-cm cosmology from the farside of the moon. *arXiv preprint arXiv:2103.05085*, 2021.

[30]Mayuri Sathyanarayana Rao, Saurabh Singh, Srivani KS, Girish BS, Keerthipriya Sathish, Raghunathan Agaram, Kavitha K, Gautam Vishwapriya, Ashish Anand, Udaya Shankar N, et al. Pratush experiment concept and design overview. *Experimental Astronomy*, 56(2):741–778, 2023.

[31]Kaan Artuc and Eloy de Lera Acedo. The spectrometer development of cosmocube, lunar orbiting satellite to detect 21-cm hydrogen signal from cosmic dark ages. *RAS Techniques and Instruments*, 4:rzae061, 12 2024.

[32]Jiacong Zhu, Eloy de Lera Acedo, Kaan Artuc, and Xuelei Chen. Rfsoc receiver calibration system for 21-cm global spectrum experiments from space: the cosmocube case. *RAS Techniques and Instruments*, 4:rzae064, 02 2025.

[33]Alan EE Rogers and Judd D Bowman. Absolute calibration of a wideband antenna and spectrometer for accurate sky noise temperature measurements. *Radio Science*, 47(06):1–9, 2012.

[34]Raul A Monsalve, Alan EE Rogers, Judd D Bowman, and Thomas J Mozdzen. Calibration of the edges high-band receiver to observe the global 21 cm signature from the epoch of reionization. *The Astrophysical Journal*, 835(1):49, 2017.

[35]Don LaFontaine. Making accurate voltage noise and current noise measurements on operational amplifiers down to 0.1 hz. *Application Note AN1560, Intersil*, 2011.

[36]Michael Steffes. Noise analysis for high speed op amps. *Burr-Brown Application Bulletin AB-103*, 1996.

[37]Harry Nyquist. Thermal agitation of electric charge in conductors. *Physical review*, 32(1):110, 1928.

[38]Jiansheng Xu, Yisong Dai, and Derek Abbott. A complete operational amplifier noise model: Analysis and measurement of correlation coefficient. *IEEE Transactions on Circuits and Systems I: Fundamental Theory and Applications*, 47(3):420–424, 2000.

[39]Gino Giusi, Felice Crupi, Calogero Pace, and Paolo Magnone. Full model and characterization of noise in operational amplifier. *IEEE Transactions on Circuits and Systems I: Regular Papers*, 56(1):97–102, 2009.

[40]Janhvi Chauhan and Usha Neelakantan. An experimental approach for precise temperature measurement using platinum rtd pt1000. In *2016 International Conference on Electrical, Electronics, and Optimization Techniques (ICEEOT)*, pages 3213–3215. IEEE, 2016.

[41]Joseph Wu. A basic guide to rtd measurements. *change*, 100(4.183):10–12, 2018.

[42]Yuan Yongliang Li Pengfei and Cao Xiang. Research on improving measurement accuracy of low temperature waste heat pump system of temperature sensor. *AIP Advances*, 13(7):075003, 07 2023.

[43]Fengquan Wu, Jixia Li, Shifan Zuo, Xuelei Chen, Santanu Das, John P. Marriner, Trevor M. Oxholm, Anh Phan, Albert Stebbins, Peter T. Timbie, Reza Ansari, Jean-Eric Campagne, Zhiping Chen, Yanping Cong, Qizhi Huang, Juhun Kwak, Yichao Li, Tao Liu, Yingfeng Liu, Chenhui Niu, Calvin Osinga, Olivier Perdereau, Jeffrey B. Peterson, John Podczerwinski, Huli Shi, Gage Siebert, Shijie Sun, Haijun Tian, Gregory S. Tucker, Qunxiong Wang, Rongli Wang, Yougang Wang, Yanlin Wu, Yidong Xu, Kaifeng Yu, Zijie Yu, Jiao Zhang, Juyong Zhang, and Jialu Zhu. The Tianlai dish pathfinder array: design, operation, and performance of a prototype transit radio interferometer. *MNRAS*, 506(3):3455–3482, September 2021.

[44]F. Wu et al. J. Li, S. Zuo. The tianlai cylinder pathfinder array: System functions and basic performance analysis. *Science China Physics, Mechanics, and Astronomy*, 63(129862), December 2020.